Supporting Information

Cryosectioning-enabled super-resolution microscopy for studying nuclear architecture at the single protein level

Supplementary Figures

Supplementary Tables

Supplementary References

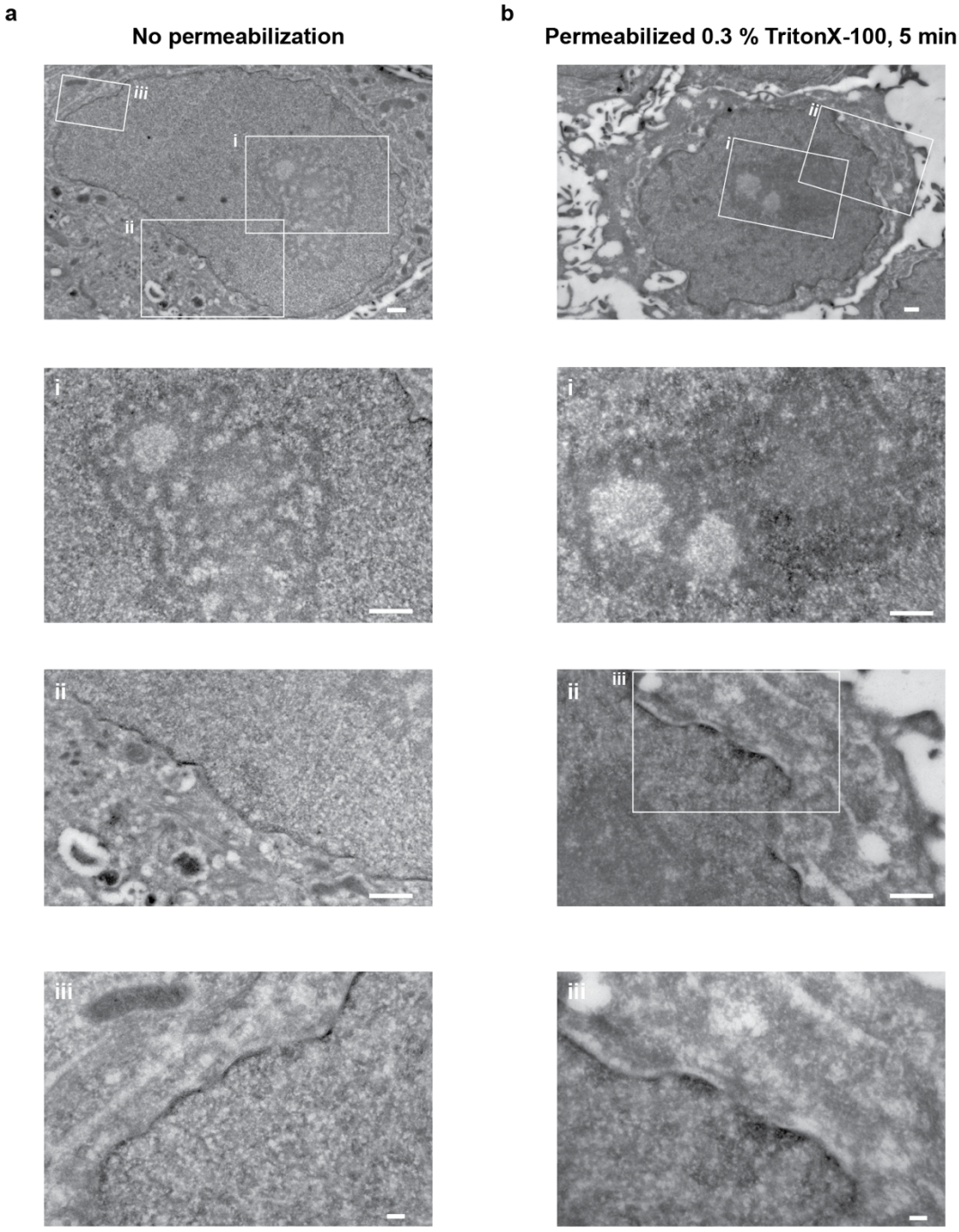

Supplementary Fig. 1 | TEM imaging confirms nuclear preservation in permeabilized cryosections. a Transmission electron microscopy (TEM) images of untreated 150 nm HeLa cryosections. Although ultrastructural studies are commonly performed in even thinner cryosection (<100 nm), the contrast is sufficient to reveal structural features within the nucleus (nucleolus, nuclear envelope, and nuclear pores) and in the cytoplasm (endoplasmic reticulum, mitochondria, and cristae). The bottom three images show magnified regions of the same cell shown in the top image. **b** TEM images of 150 nm cryosections that were permeabilized with 0.3 % TritonX-100 for 5 min. As expected, detergent treatment affects lipids and membrane structures and results in observable extraction especially from the cytoplasmic domain. Overall, the intranuclear space, chromatin as well as the nucleolus appear ultrastructurally preserved. The bottom three images show magnified regions of the same cell shown in the top image. Scale bars, 500 nm, except 100 nm in (**a**iii and **b**iii).

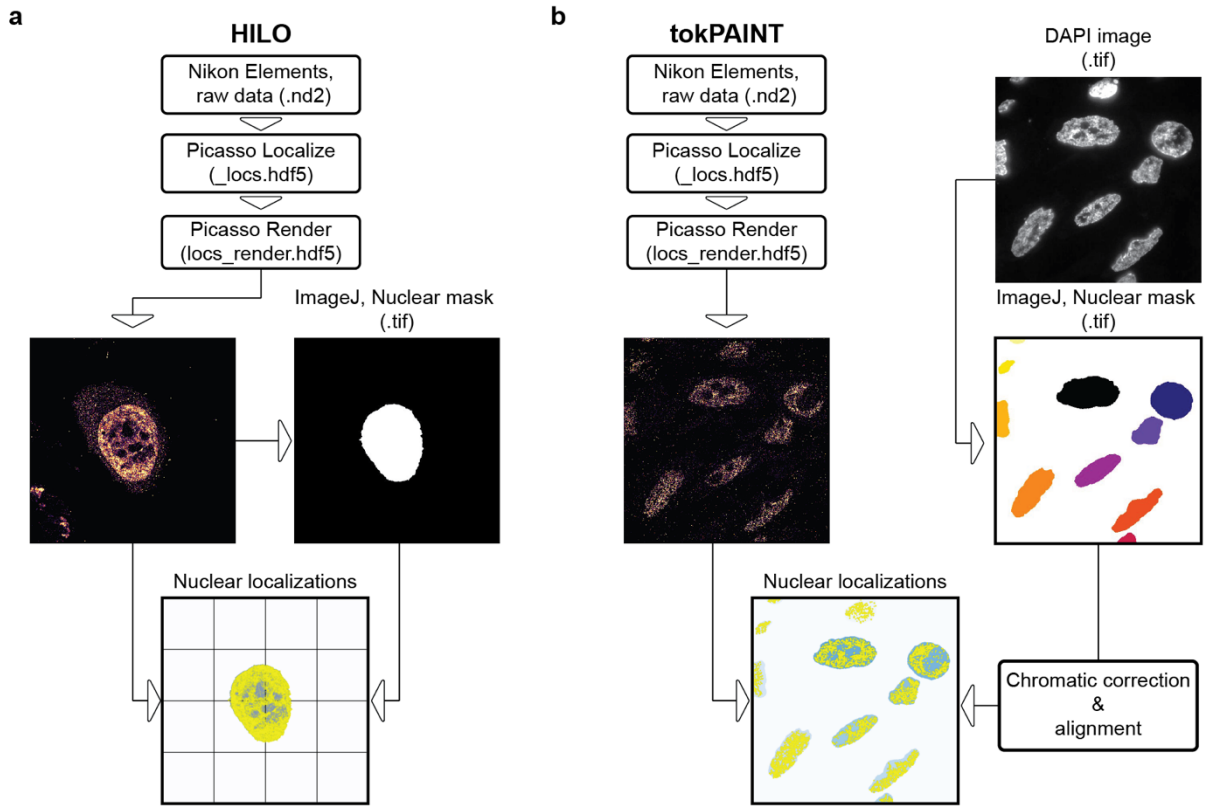

Supplementary Fig. 2 | Segmentation of nuclear localizations for HILO and tokPAINT. a Workflow for nuclear segmentation in HILO DNA-PAINT imaging. Raw time series were recorded using Nikon Elements and processed with Picasso Localize software module[1]. The localization files were subsequently loaded into Picasso Render[1] to perform drift correction (global correction via redundant-cross correlation[2] and subsequent correction based on fiducials) and saved. From Picasso Render we further exported a low-resolution and oversaturated image, that we used to create a nuclear mask via FIJI[3] (thresholding to create a mask & the plugin BIOP/Image Analysis/ROIs/ ROIs to label image to export a binary mask as .tif file. https://github.com/BIOP). Using a custom Python script, both the drift corrected localization file and the binary mask were loaded to filter for nuclear localizations based on the mask. Note: we did not use DAPI staining for nuclear segmentation as in tokPAINT due to poor image quality in HILO illumination. **b** Workflow for nuclear segmentation in tokPAINT imaging. Data acquisition, localization and drift correction were performed as in a. Prior to each tokPAINT experiment, we acquired a single DAPI image for later nuclear segmentation. For each tokPAINT experiment, a corresponding binary mask was created out of the DAPI image analogously to a. We performed an affine transformation using Fiji[3] for descriptor-based registration[4] based on TetraSpeck™ multicolor bead images. Although chromatic aberrations were negligible, this provided us with the option to transform the DAPI channel mask with respect to the tokPAINT color channel. Lastly, the same custom Python script was used to correct for a potential offset due to sample drift during the tokPAINT acquisition and to subsequently filter for all nuclear localizations accordingly. All images shown have dimension 66.6 µm x 66.6 µm.

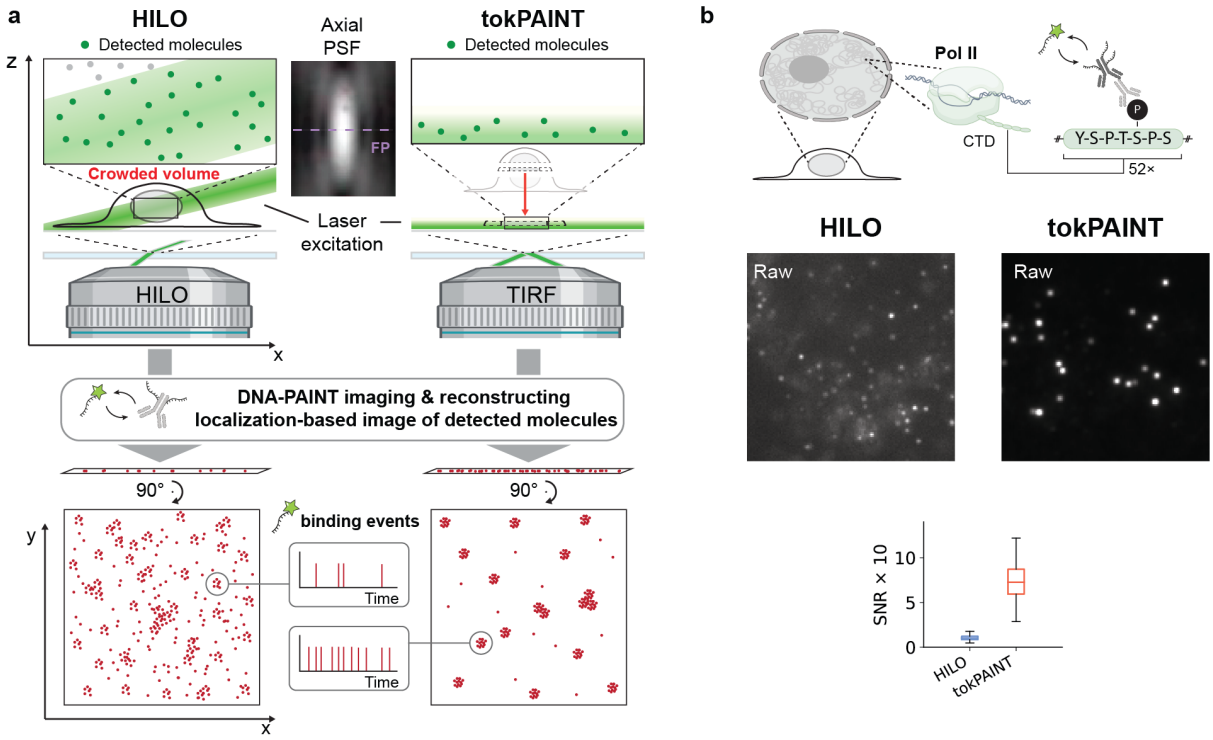

Supplementary Fig. 3 | Influence of the detection volume in DNA PAINT imaging of dense targets. a Schematic comparing the detection volumes of HILO (highly inclined laminated optical sheet[5]) nuclear DNA-PAINT imaging and tokPAINT imaging at the example of highly abundant targets such as Pol II. Physical sectioning 'de-crowds' the detection volume and enables DNA-PAINT imaging under improved signal to noise conditions and, hence, at improved resolution. Since imager binding needs to be sparse for truthful super-resolution reconstruction, a smaller number of detected target molecules allows operating at higher imager binding frequencies per molecule compared to the larger detection volume where binding events need to be divided over the larger molecule number. Furthermore, the smaller detection volume in tokPAINT can reduce the influence of non-specific localizations[6] populating the image. Please refer to **Note for intranuclear HILO DNA-PAINT imaging** in **Supplementary Fig. 4** for a detailed discussion of quantitative nuclear DNA-PAINT via HILO. **b** Comparing the signal-to-noise ratios measured for nuclear localizations in HILO vs. tokPAINT Pol II S5p data sets that are shown in **Fig. 1**.

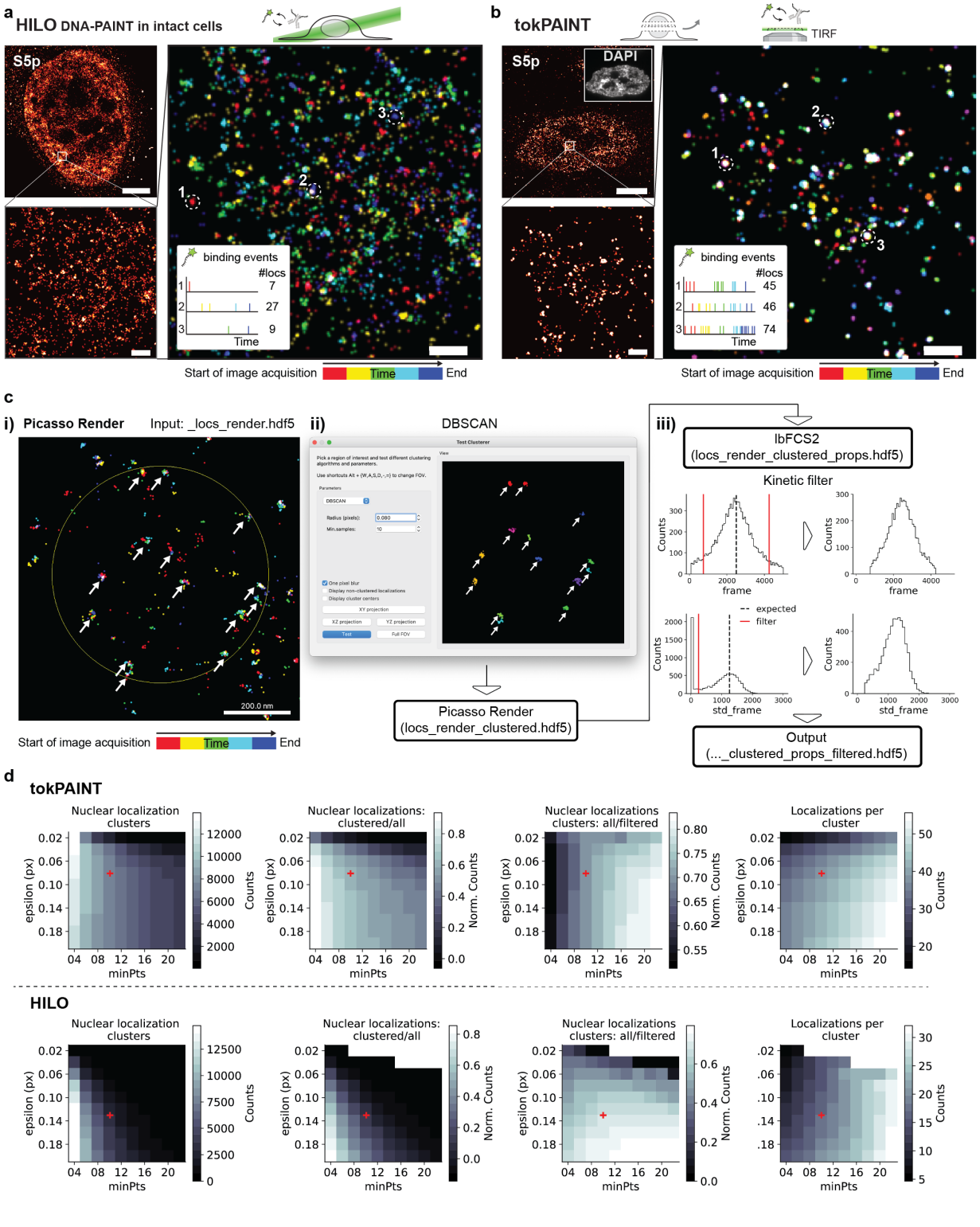

Supplementary Fig. 4 | Choice of DBSCAN clustering parameters and filtering pipeline. a Same HILO DNA-PAINT image as shown in **Fig. 1**c, but localizations in the zoom-in were color-coded according to registration time during data acquisition. The crowded image of discretely colored localizations indicates that with HILO illumination in intact cells it is not possible to easily distinguish non-specific sticking events of imager strands (appearing in a single color only) from repetitive signal (overlapping colors from multiple binding events separated in time). **b** Same as a, but for tokPAINT data set in shown in **Fig. 1**d. The higher localization precision yields sparse and discernible localization clusters, of which many are revealed by temporal coloring as repetitive 'white-

colored' localization clusters, demonstrating that meaningful kinetic information can be leveraged for identifying specific signal DNA-PAINT signal. **c** Clustering and filtering workflow. In this study, we used the DBSCAN (Density-based spatial clustering of applications with noise) algorithm[7] implementation in Picasso Render[1] for cluster identification. The Render module "Test Clusterer" tests the clustering outcome for a specific region given the parameter choices of DBSCAN epsilon (distance between points to be considered as within neighborhood) and minPts (number of points required to form a dense region) (i-ii). Note that Render refers to epsilon as 'radius' and to Min.Pts as 'Min.samples' (ii). The kinetic color coding offers the advantage to adjust both parameters such that individual specific localization clusters carrying overlapping localizations of multiple colors were each assigned to one cluster. Running DBSCAN allowed us to export localization clusters for further processing exploiting our previously developed Python modules (picasso_addon[8], lbFCS[9] and lbFCS2[10]). Here, we performed kinetic filtering discarding localization clusters with (iii): mean(frame) < 0.85 x M/2 or mean(frame) > 1.15 x M/2, std(frame) < 0.1 x M and a mean dark time[11] τ_D < 0.8 M; where M is the total number of frames in the data set. **d** Parameter scan for DBSCAN comparing tokPAINT and HILO data sets in **Fig. 1**c and d (top and bottom, respectively). The red plus sign indicates the chosen parameter. Scan results are displayed for the following quantities: total number of identified nuclear localization clusters, the ratio of nuclear localizations that could be assigned to a localization cluster compared to all nuclear localizations, the ratio of filtered vs. unfiltered localization clusters and the number of localizations per cluster. In general, this scan confirms the considerations outlined in **Supplementary Fig. 3** that for dense targets such as Pol II lower localization precision and sparser binding in HILO reduces the ability of cluster identification for the same acquisition lengths as chosen for tokPAINT (~25 min). It also shows how the analysis results in the vicinity of the chosen parameters in tokPAINT had minor effects on the analysis output. Scale bars, 5 µm in (**a**,**b**), 400 nm in zoom-ins.

Note for intranuclear HILO DNA-PAINT imaging. For extended image acquisition times (e.g. >70 min[12]), it is possible to enhance clusterability for nuclear DNA-PAINT data also for HILO acquisitions of dense targets[12–14]. Clusterability can further be improved by performing 'computational sectioning' of 3D HILO DNA-PAINT data sets, e.g. by considering only localizations within 120 nm in z around the focal plane[12]. However, extended data acquisitions have no effect on the reduced resolution in HILO compared to TIRF, which also in previous studies was in the range of tens of nanometers[12,14] and did not allow to visualize individual docking strand-conjugated antibodies. There are several options to increase the achievable resolution also in HILO, however, likely not leading to the resolution achievable with TIRF. Fluorogenic imagers[15] that only fluorescence upon binding to docking strands can reduce background fluorescence and prevent bleaching of freely-diffusing imagers[13]. Repetitive docking strand designs allow imaging at lower imager concentrations, further reducing fluorescence background. Left-handed imager and docking strands have further shown to reduce non-specific binding in the context of nuclear DNA-PAINT[16], likely improving image quality for larger imaging volume in HILO. **RESI**. Lastly, we would like to highlight a recently-developed, celver scheme termed resolution enhancement by sequential imaging[17] (RESI), that circumvents the limited resolution of HILO DNA-PAINT imaging via sequential imaging. Essentially performing Exchange-PAINT[18] on the same target of interest by e.g. using a mixture of nanobodies against the same epitope, but each conjugated with an orthogonal docking strand sequence, it is possible to 'de-crowd' the detection volume in sequential imaging rounds. The goal of RESI is to record DNA-PAINT images where each localization cluster arises from a single docking strand alone and whose localizations are hence approximately Gaussian distributed. A second round of 'localizing the center of each localization cluster' enables to determine docking strand anchor points at down to Ångstrom precision. As in Exchange-PAINT, the full image can be reconstructed by subsequentially merging of all sequential rounds[17]. Thus, for four rounds of HILO DNA-PAINT imaging of nuclear pore complexes at moderate initial resolutions of >15 nm, RESI postprocessing led to localization precision 5 Å and resolving distances between nucleoporins between 5-10 nm[17]. While this strategy poses an extremely powerful approach, imaging of dense target structures might become expensive in terms of number of nanobody conjugations and imaging rounds per experiment. Here, we see an additional advantage of cryosectioning that could keep the number of required imaging rounds low for RESI imaging.

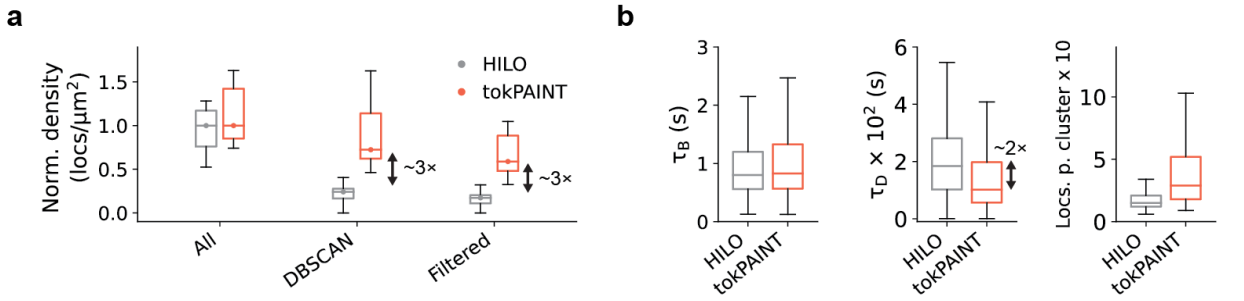

Supplementary Fig. 5 | Comparison of binding kinetics for HILO and tokPAINT. a. Normalized density of nuclear localizations (all), after applying DBSCAN clustering and kinetic filtering for tokPAINT and HILO data sets shown in **Fig. 1**c-d. **b** Imager binding kinetics measured per localization clusters and number of localizations per cluster. The average binding time of an imager is referred to as 'bright time' or τ_B and the average duration in between consecutive imager binding events is referred to as 'dark time' or τ_D.

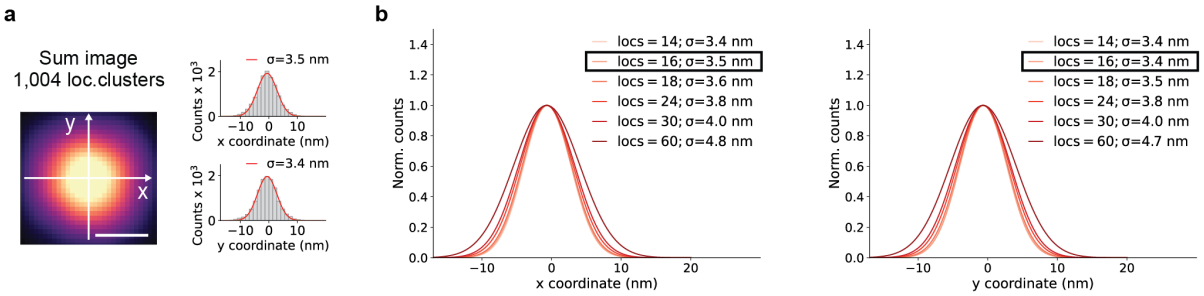

Supplementary Fig. 6 | Scan for minimum number of localizations per cluster – HeLa cells. a Center-of-mass aligned sum image of localization clusters with 16 or less localizations and line plots along the indicated axes (white arrows). **b** Parameter scan showing that a further reduction of the maximum number of localizations per cluster does not influence the distribution width within localization clusters, indicating a regime governed by localization precision. The overall width is in agreement with the physical size of DNA-conjugated antibodies. Scale bars, 5 nm.

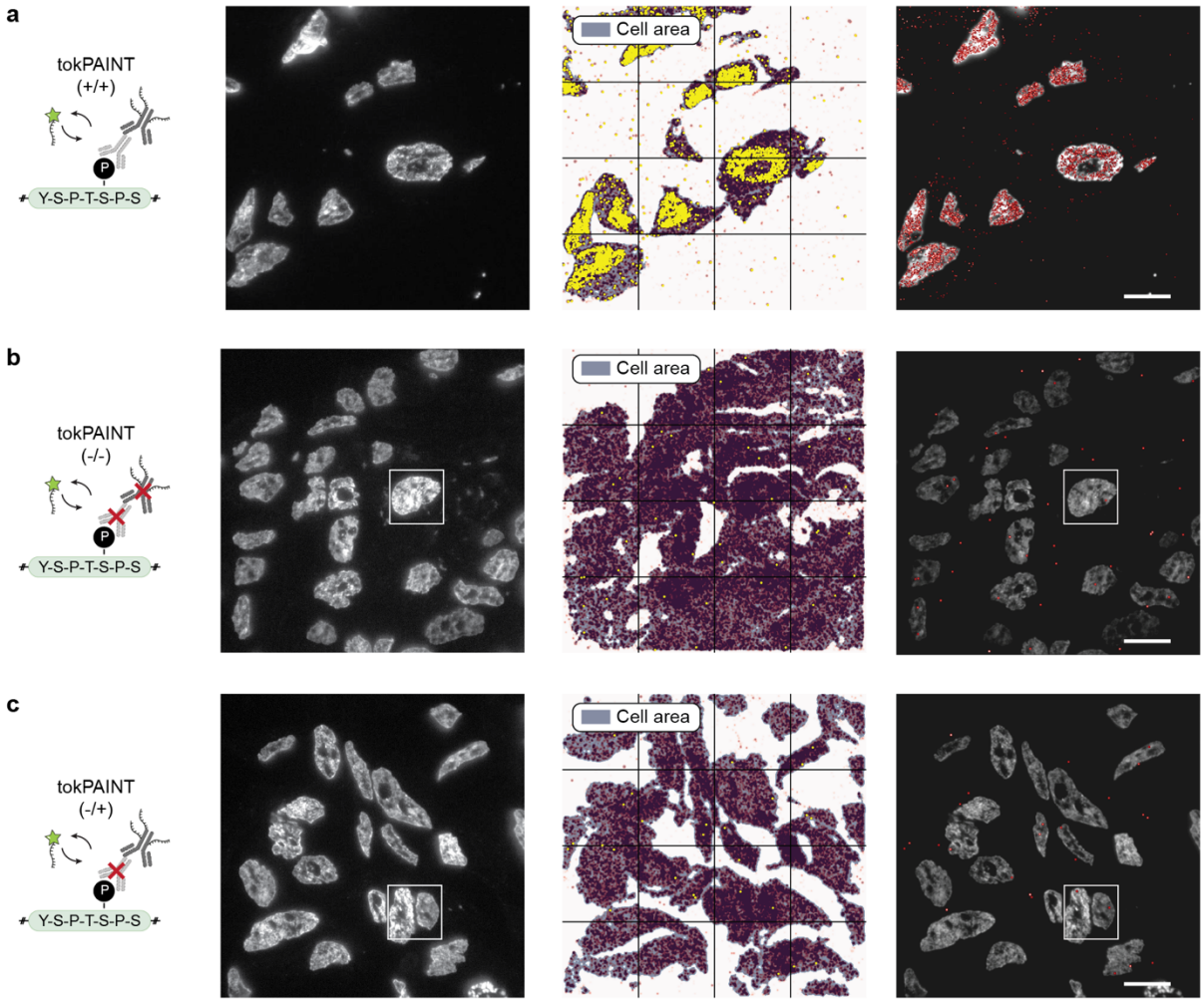

Supplementary Fig. 7 | tokPAINT negative controls. a. Indirect tokPAINT Pol II S5p data set, showing DAPI (left image). Center: all identified localization clusters after kinetic filtering (yellow) overlayed with a binary mask marking sectioned cells (blue). Right: same as center, but localization clusters colored in red and overlayed with the DAPI image. The binary mask for the cell areas was generated as described in Supplementary Fig. 2 but exporting an oversaturated and low-resolution image from all localizations in Picasso render. **b** Same as a, except for the negative control that was conducted under identical conditions as a, but without addition of both antibodies during sample preparation. The cell area was used to calculate the overall localization cluster density, and the white box indicates the nucleus shown in Fig. 2b, top. **c** Same as b, except for the negative control that was conducted under identical conditions as a , but without addition of primary antibodies but subsequent incubation of DNA-conjugated secondary antibodies during sample preparation. The cell area was used to calculate the overall localization cluster density and the white box indicates the nucleus shown in Fig. 2b, bottom. Scale bars, 10 µm.

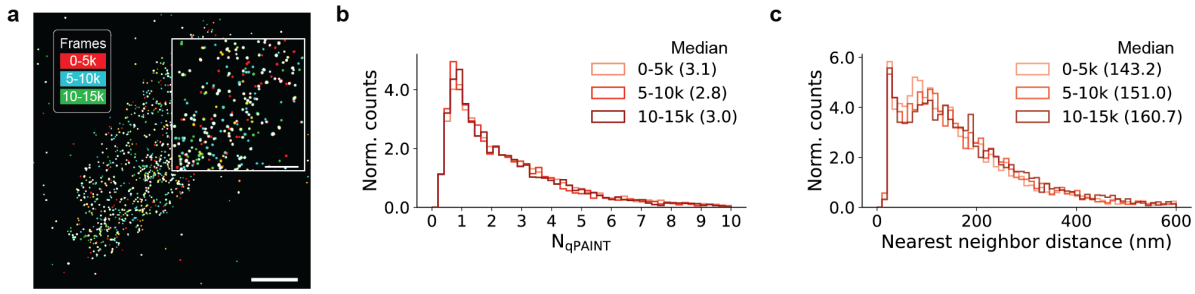

Supplementary Fig. 8 | tokPAINT quantifications for extended image acquisition times. a. tokPAINT Pol II S5p data set acquired for 15,000 frames, i.e. 3x longer than previous tokPAINT data sets. The image was split into 3x 5,000 frame subsets and displayed as multicolor overlay (red first - 5,000 frames, blue - second 5,000 frames and green - last 5,000 frames). The high fraction of multicolor and white localization clusters indicates good sample preservation. **b** Histogram of N_{qPAINT} counting results from all three temporal segments indicating a negligible effect of imaging time. **c** Histogram of nearest neighbor distances between localization clusters over all three segments. A minor reduction (~5 %) per 5,000 frames could potentially be due to photoinduced docking strand depletion[19]. Scale bars, 3 µm in (**a**) and 1 µm in zoom-in.

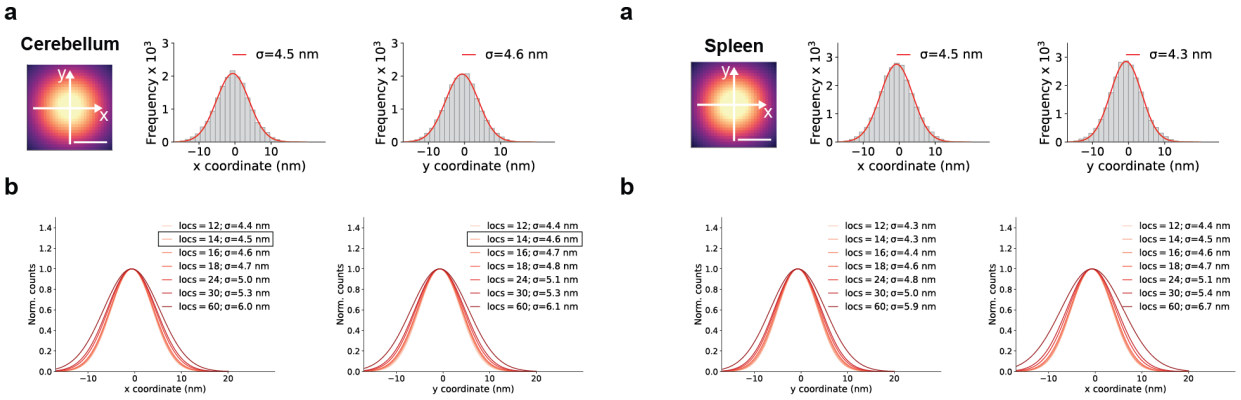

Supplementary Fig. 9 | Scan for minimum number of localizations per cluster – tissue tokPAINT. a Center-of-mass aligned sum image of localization clusters with 16 or less localizations and line plots along the indicated axes (white arrows). **b** Parameter scan showing that a further reduction of the maximum number of localizations per cluster does not influence the distribution width within localization clusters, indicating a regime governed by localization precision. The overall width is in agreement with the physical size of DNA-conjugated antibodies. Scale bars, 5 nm.

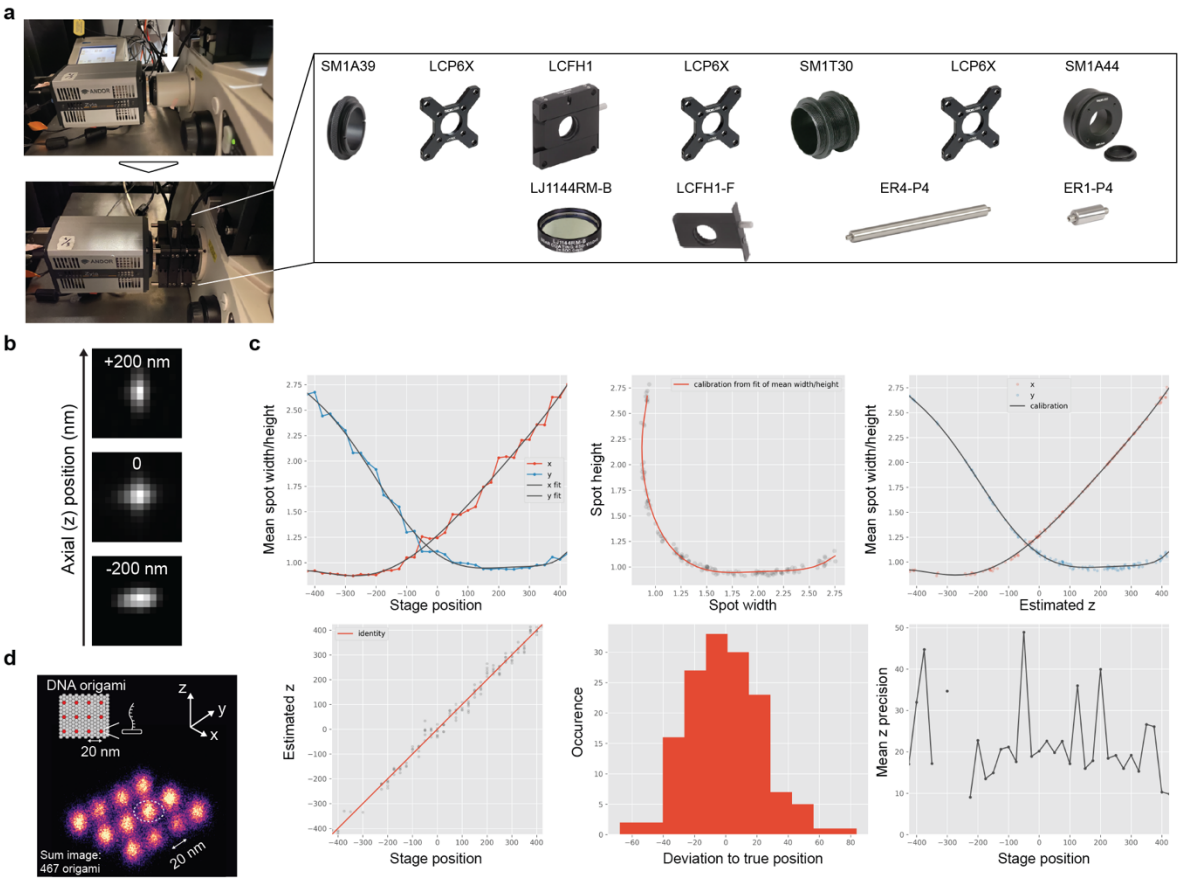

Supplementary Fig. 10 | Custom cylindrical lens insertion for 3D tokPAINT. a Parts list of Thorlabs optics components to replace the C-mount port (white arrow) at our standard Nikon TI Eclipse TIRF system with a cylindrical lens inset. Approximate cost at the time this manuscript was written: ~700 $. Part LCFH1-F can be purchased extra to leave an empty lens holder at the microscope for standard TIRF microscopy. The threaded tubing and our general design allow a flexible adjustment of the total distance between the camera and the port to match the focal length of the tube lens. **b** Axial calibration z-stack acquired using fluorescent beads. **c** Picasso Localize[1] output of 3D calibration: the z-stack was acquired at a step size of 25 nm and then loaded into Picasso Localize[1]. Running "Calibrate 3D", a box size large enough to fit the enlarged astigmatic point spread function was chosen. The generated 3D calibration .yaml file can be loaded when localization a 3D data set, and the option "Fit z" needs to be ticket. Importantly, since insertion of an additional lens affects the magnification, this can be compensated for in Picasso. In our case, we determined the magnification factor by using DNA origami that carried a pre-designed 20 nm spacing as a nano ruler (**d**).

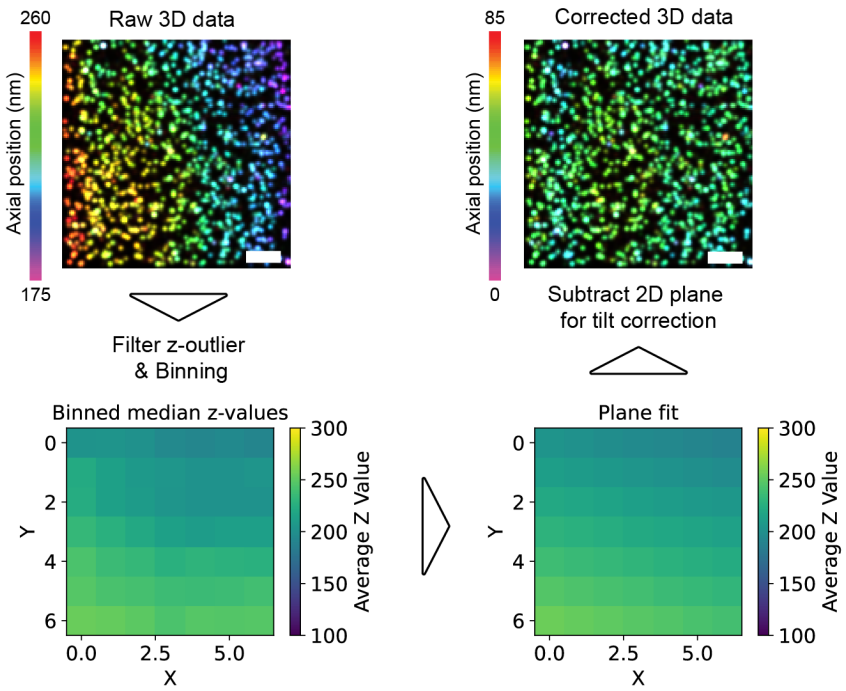

Supplementary Fig. 11 | Planar fit for axial tilt-correction in 3D tokPAINT. Axial tilt correction workflow shown at the example of a DNA origami 3D DNA-PAINT set using a custom Python implementation inspired by ref.[20]. After removal of z-outliers (>4x median) the 3D data set was binned into a pixelated map where each pixel was assigned the median z-position of all localizations within the pixel. Next a 2D plane was fit to the pixel map to approximate any tilt. Lastly, the planar fit was subtracted from the initial 3D tokPAINT data set to remove axial tilt and normalize to z=0.

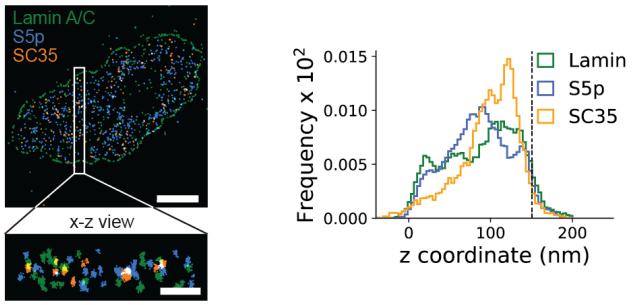

Supplementary Fig. 12 | Axial distribution of antibody signal for 3D Exchange-tokPAINT. Axial distribution of antibody signal for 3D Exchange-tokPAINT (Lamin A/C, POL II Pol II S5p and SC35) displayed in **Fig. 5**c. The dashed line indicates the set cutting thickness of 150 nm. Scale bars, 3 μm in (**a**) and 150 nm in zoom-in.

Supplementary Table 1 | Imaging parameters for tokPAINT/DNA-PAINT

Figure	Sample, (blocking buffer in PBS)	Labeling (dilution; incubation time)	Docking strand sequence	Imager concentration (nM)	Imaging Buffer	Laser power behind objective (mW)	Exposure time (ms)	Frames
1c S2-5	HeLa, whole cells, (3% BSA + 0.25% Triton-X 100)	Rabbit Pol II S5p (1:200; overnight) + Donkey a-rabbit (1:200; 60min)	P1	~500 pM	C	~20	200	5,000
1d 2a,d,e,f Ext. Dat. 2 S2-6, S8*	HeLa, cryosection, (0.5% BSA + 0.2% gelatin)	Rabbit Pol II S5p (1:200; 15min) + Donkey a-rabbit (1:200; 15min)	P1	~500 pM	C	~16	200	5,000 *(3x extended 15,000)
2b, top S7	HeLa, cryosection (1% gelatin)	-	-	~500 pM (P1)	C	~16	200	5,000
2b, bottom S7	HeLa, cryosection (1% gelatin)	Donkey a-rabbit (1:200; 10min)	P1	~500 pM	C	~16	200	5,000
2c, top	HeLa, cryosection (1% gelatin)	*Not phosphatase treated.* Rabbit Pol II S5p (1:200; 10min) + Donkey a-rabbit Alexa 488	-	-	-	-	-	1
2c, bottom	HeLa, cryosection (1% gelatin)	*Phosphatase treated.* Rabbit Pol II S5p (1:200; 10min) + Donkey a-rabbit Alexa 488	-	-	-	-	-	1
2e, qPAINT S7	HeLa, cryosection (1% gelatin)	Rabbit Pol II S5p (1:200; 10min) + Donkey a-rabbit (1:200; 10min)	R4	~25 pM	C	~16	100	9,000
2e, qPAINT	HeLa, cryosection (1% gelatin)	Rabbit Pol II S5p (1:50; 15min)	R3	~50 pM	C	~16	100	9,000
2e, qPAINT	HeLa, cryosection (1% gelatin)	Rabbit Pol II S5p (1:100; 15min)	R3	~250 pM	C	~16	100	4,000
3a top, S9	Mouse cerebellum, cryosection (3% BSA)	Rabbit Pol II S5p (1:100; 20min) + Donkey a-rabbit (1:100; 20min)	P1	~500 pM	C	~8	200	5,000

Figure	Sample, (blocking buffer in PBS)	Labeling (dilution; incubation time)	Docking strand sequence	Imager concentration (nM)	Imaging Buffer	Laser power behind objective (mW)	Exposure time (ms)	Frames
3a bottom, S9	Mouse spleen, cryosection (3% BSA)	Rabbit Pol II S5p (1:100; 20min) + Donkey a-rabbit (1:100; 20min)	P1	~500 pM	C	~8	200	5,000
4b Ext. Dat. 3	HeLa, cryosection (0.5% BSA + 0.2% gelatin)	Mouse LaminA/C - R2 Rabbit Pol II S5p - R3 Mouse SC35 - R4 (all 1:200; overnight)	R2 R3 R4	~500 pM ~500 pM ~1,000 pM	C	~24	100	6,000
4c	HeLa, cryosection (3% BSA)	Rabbit a-tubulin (1:200; overnight) Telomer FISH probe	P1	~100 pM	C	~24	150	5,000
4d	HeLa, cryosection (1% gelatin)	Poly(dT)-digoxigenin Mouse a-digoxigenin (1:100; 15 min) Goat a-mouse (1:100; 15 min)	P1	~500 pM	C	~8	100	10,000
5a,b, S10, S11 (3D imaging)	DNA origami	-	Pm2	~500 pM	C	~16	100	6,000
5c (3D imaging)	HeLa, cryosection (0.5% BSA + 0.2% gelatin)	Mouse LaminA/C (R2) Rabbit Pol II S5p (R3) Mouse SC35 (R4) (all 1:200; overnight)	R2 R3 R4	~500 pM ~500 pM ~500 pM	C	~24	100	6,000
Ext. Dat. 1	DNA origami	-	R3	~500 pM	C	~16	100	9,000
S7	HeLa, cryosection (1% gelatin)	Rabbit Pol II S5p (1:200; 10 min) + Donkey a-rabbit (1:200; 10 min)	P1	~500 pM	C	~16	200	5,000

Supplementary Table 2 | Used DNA-PAINT sequences

Imager-Docking ID	Docking sequence	Imager sequence
P1	ttATACATCTA	CTAGATGTAT-Cy3b
Pm2	ttTCTTCTTCTTCTTCTTCTTCTTCTTCTTCT	GAGGAGG-Cy3b
R2	ttACCACCACCACCACCACCA	TGGTGGT-Cy3b
R3	ttCTCTCTCTCTCTCTCTCTC	GAGAGAG-Cy3b
R4	ttACACACACACACACACACA	TGTGTGT-Cy3b

Supplementary References

1. Schnitzbauer, J., Strauss, M. T., Schlichthaerle, T., Schueder, F. & Jungmann, R. Super-resolution microscopy with DNA-PAINT. *Nature Protocols* **12**, 1198 (2017).
2. Wang, Y. *et al.* Localization events-based sample drift correction for localization microscopy with redundant cross-correlation algorithm. *Opt. Express, OE* **22**, 15982–15991 (2014).
3. Schindelin, J. *et al.* Fiji: an open-source platform for biological-image analysis. *Nat Methods* **9**, 676–682 (2012).
4. Preibisch, S., Saalfeld, S., Schindelin, J. & Tomancak, P. Software for bead-based registration of selective plane illumination microscopy data. *Nat Methods* **7**, 418–419 (2010).
5. Tokunaga, M., Imamoto, N. & Sakata-Sogawa, K. Highly inclined thin illumination enables clear single-molecule imaging in cells. *Nature Methods* **5**, 159 (2008).
6. Clowsley, A. H. *et al.* Repeat DNA-PAINT suppresses background and non-specific signals in optical nanoscopy. *Nature Communications* **12**, 1–10 (2021).
7. Ester, M., Kriegel, H.-P., Sander, J. & Xu, X. A Density-Based Algorithm for Discovering Clusters in Large Spatial Databases with Noise. *Proceedings of the 2nd International Conference on Knowledge Discovery and Data Mining* 226–231 (1996).
8. Stehr, F. *et al.* Tracking single particles for hours via continuous DNA-mediated fluorophore exchange. *Nature Communications 2021 12:1* **12**, 1–8 (2021).
9. Stein, J. *et al.* Toward Absolute Molecular Numbers in DNA-PAINT. *Nano Letters* **19**, 8182–8190 (2019).
10. Stein, J., Stehr, F., Jungmann, R. & Schwille, P. Calibration-free counting of low molecular copy numbers in single DNA-PAINT localization clusters. *Biophysical Reports* **1**, 100032 (2021).
11. Jungmann, R. *et al.* Single-Molecule Kinetics and Super-Resolution Microscopy by Fluorescence Imaging of Transient Binding on DNA Origami. *Nano Letters* **10**, 4756–4761 (2010).
12. Otterstrom, J. *et al.* Super-resolution microscopy reveals how histone tail acetylation affects DNA compaction within nucleosomes in vivo. *Nucleic acids research* **47**, 8470–8484 (2019).
13. Schueder, F. *et al.* Unraveling cellular complexity with unlimited multiplexed super-resolution imaging. 2023.05.17.541061 Preprint at https://doi.org/10.1101/2023.05.17.541061 (2023).
14. Castells-Garcia, A. *et al.* Super resolution microscopy reveals how elongating RNA polymerase II and nascent RNA interact with nucleosome clutches. *Nucleic Acids Research* **50**, 175–190 (2022).
15. H Chung, K. K. *et al.* Fluorogenic DNA-PAINT for faster, low-background super-resolution imaging. *Nature Methods* (2022) doi:10.1038/s41592-022-01464-9.
16. Geertsema, H. J. *et al.* Left-handed DNA-PAINT for improved super-resolution imaging in the nucleus. *Nature Biotechnology* 1–4 (2021) doi:10.1038/s41587-020-00753-y.
17. Reinhardt, S. C. M. *et al.* Ångström-resolution fluorescence microscopy. *Nature* **617**, 711–716 (2023).
18. Jungmann, R. *et al.* Multiplexed 3D cellular super-resolution imaging with DNA-PAINT and Exchange-PAINT. *Nat Methods* **11**, 313–318 (2014).
19. Blumhardt, P. *et al.* Photo-Induced Depletion of Binding Sites in DNA-PAINT Microscopy. *Molecules* **23**, 3165 (2018).
20. Franke, C. *et al.* Approach to map nanotopography of cell surface receptors. *Commun Biol* **5**, 1–16 (2022).